mathematics

MDPI

Article

Transient Dynamic Response Analysis of Two-Dimensional Saturated Soil with Singular Boundary Method

Dongdong Liu [1], Xing Wei [1,*], Chengbin Li [2], Chunguang Han [2], Xiaxi Cheng [1] and Linlin Sun [3,*]

[1] Jiangxi Key Laboratory of Disaster Prevention, Mitigation and Emergency Management, School of Civil Engineering & Architecture, East China Jiaotong University, Nanchang 330013, China
[2] China Railway Construction Bridge Engineering Bureau Group Co., Ltd., Tianjin 300000, China
[3] School of Science, Nantong University, Nantong 226019, China
* Correspondence: weix911@126.com (X.W.); rudong9110@163.com (L.S.); Tel.: +86-791-87046046 (X.W.); +86-513-55003300 (L.S.)

Abstract: In this paper, the singular boundary method (SBM) in conjunction with the exponential window method (EWM) is firstly extended to simulate the transient dynamic response of two-dimensional saturated soil. The frequency-domain (Fourier space) governing equations of Biot theory is solved by the SBM with a linear combination of the fundamental solutions. In order to avoid the perplexing fictitious boundary in the method of fundamental solution (MFS), the SBM places the source point on the physical boundary and eliminates the source singularity of the fundamental solution via the origin intensity factors (OIFs). The EWM is carried out for the inverse Fourier transform, which transforms the frequency-domain solutions into the time-domain solutions. The accuracy and feasibility of the SBM-EWM are verified by three numerical examples. The numerical comparison between the MFS and SBM indicates that the SBM takes a quarter of the time taken by the MFS.

Keywords: singular boundary method; meshless methods; exponential window method; saturated soil; transient dynamic response analysis

MSC: 65N35; 65N80; 74H15

Citation: Liu, D.; Wei, X.; Li, C.; Han, C.; Cheng, X.; Sun, L. Transient Dynamic Response Analysis of Two-Dimensional Saturated Soil with Singular Boundary Method. *Mathematics* **2022**, *10*, 4323. https://doi.org/10.3390/math10224323

Academic Editor: Ravi P. Agarwal

Received: 27 October 2022
Accepted: 15 November 2022
Published: 17 November 2022

1. Introduction

The transient dynamic analysis is of great importance in the geotechnical and mechanical engineering to observe the time-history mechanical response caused by the dynamic loads [1,2]. Although there are some analytical solutions for the regular geometric shapes with isotropic and homogeneous material properties and simple boundary conditions, the numerical tools are usually more flexible and effective for general real-world problems. The transient analysis is usually divided into two parts, viz. spatial discretization and temporal discretization.

For the spatial discretization, the finite element method (FEM) is one of most powerful numerical methods. In light of its theoretical completeness and well-established commercial software, the FEM is robust to different engineering applications [3,4]. Nevertheless, the FEM requires the artificial boundary [5] to analyze the infinite and semi-infinite medium. Besides the FEM, the other domain-type methods [6] encounter the same difficulty. The boundary element method (BEM) has been boosted as an effective alternative in infinite and semi-infinite problems because the fundamental solutions used in the BEM automatically satisfy the Sommerfield radiation condition at infinity. The utilization of the fundamental solutions makes the BEM avoid domain discretization, because the kernel function satisfies governing equations. The superiority of the BEM motivated researchers to develop novel numerical methods based on analytical solutions, such as the fundamental solutions [7–9], the general solutions [10–12] and the particular solutions [13–16]. Among them, most

of numerical methods are pertinent to the fundamental solutions, including the method of fundamental solutions (MFS) [8,17], modified method of fundamental solutions [18] and singular boundary method (SBM) [19–21], to just name a few. The SBM was firstly proposed by Chen [19] with introducing the concept of the origin intensity factor (OIF) to desingularize the fundamental solutions. Originally, the OIF was evaluated via a tedious inverse interpolation technique [22]. Later, simple analytical and empirical formulas were developed and extended the application of the SBM to different problems [23–32]. The abovementioned boundary-type methods required expensive operation counts and memory storage in real-world large-scale problems. This promotes the development of fast algorithms accelerated techniques [33–37] and localized methods [38–41]. It is worth noting that the localized variant of the boundary-type method is a domain-type method.

To implement the transient analysis, the boundary methods require special treatment to deal with time-dependent terms, including the direct time integration methods [42–44], transform methods [45–47] and time-domain fundamental solutions [48]. Except the transform method, the other methods require a proper time-step for numerical stability. Nevertheless, the long-time solution may deteriorate as the time increases. The Krylov deferred correction method (KDC) [49] allows larger time step size for the long-time analysis with acceptable temporal accumulation errors. In the transform methods, the frequency-domain governing equation is solved at some discrete sampling frequencies, and then the frequency-domain solutions are transformed back to the time-domain solutions via the inverse transform, namely the Laplace transform or Fourier transform. The inverse transform is carried out by numerical methods, which may consume a lot of time. The Fourier transform is more attractive because its inverse process can be accelerated by the fast Fourier transform (FFT). However, in lightly damped systems or undamped systems, the FFT is inefficient, or even not applicable without the desired attenuation. This problem was circumvented by introducing an artificial damping to the system by the exponential window method (EWM) [50].

There are few works related to the transient dynamic response analysis of saturated soil. In this study, the SBM in conjunction with the EWM is firstly established to solve the transient dynamic problems in two-dimensional saturated soil. The SBM is formulated in the frequency domain (Fourier space). Thanks to the fundamental solutions, the SBM can be directly applied to finite-, semi-infinite and infinite domains. The source singularity of the fundamental solution is bypassed with simple formulas. Subsequently, the frequency-domain SBM solutions are transformed by the EWM. The selection of the parameters in the EWM will be discussed. The stability and accuracy of the SBM will be investigated via three numerical examples.

2. Governing Equations

For the saturated soil, it is better to take the coupling effect of two phases into consideration [51,52]. Thus, the coupling effect is taken into account in the constitute equation [53,54]:

$$\sigma_{ij} = \lambda\delta_{ij}u_{k,k} + 2\mu\varepsilon_{ij} - \alpha\delta_{ij}p,\ i = 1,3, j = 1,3, \tag{1}$$

$$p = -\alpha M u_{i,i} - M w_{i,i}, \tag{2}$$

where σ_{ij} is the effective stress; δ_{ij} the Kronecker delta; $\varepsilon_{ij} = \left(u_{i,j} + u_{j,i}\right)/2$ the strain tensor; w_i the fluid displacement with respect to the solid skeleton; p the pore pressure; u_i the average skeleton displacement; λ and μ the solid skeleton Lamé constants; and α and M the Biot parameters describing the compressibility of the fluid-saturated two-phase material.

Taking Equations (1) and (2) into the equilibrium equations, we obtained the equations of motion for the bulk porous medium and the pore fluid without body forces as [53,54]

$$\mu u_{i,jj} + \left(\lambda + \alpha^2 M + \mu\right)u_{j,ji} + \alpha M w_{j,ji} = \rho\ddot{u}_i + \rho_f\ddot{w}_i, \tag{3}$$

$$\alpha M u_{j,ji} + M w_{j,ji} = \rho_f\ddot{u}_i + m\ddot{w}_i + \frac{\eta}{k}K(t) * \dot{w}_i, \tag{4}$$

where a dot ($\bullet$) denotes the time derivative and a star ($*$) denotes the time convolution; $\rho = (1-\phi)\rho_s + \phi\rho_f$ is the density of the saturated poroelastic medium; ρ_s and ρ_f are the density of the skeleton and fluid; ϕ the porosity; η the viscosity of the pore fluid; k the permeability of the saturated poroelastic medium; $m = \alpha_\infty \rho_f / \phi$; α_∞ is the tortuosity; and $K(t)$ is a time-dependent viscosity correction factor which describes the transition between the viscous flow in the low-frequency range and the inertia-dominated flow in the high-frequency range.

The initial boundary conditions and boundary conditions are given as

$$\boldsymbol{u}^s|_{t=0} = \left.\frac{\partial \boldsymbol{u}^s}{\partial t}\right|_{t=0} = 0,\ \boldsymbol{w}|_{t=0} = 0, \text{ and } p|_{t=0} = 0, \tag{5}$$

$$u_i^s = \hat{u}_i^s, \text{ on } \Gamma_u^s, \tag{6}$$

$$t_i^s = \sigma_{i1}^s n_1 + \sigma_{i3}^s n_3 = \hat{t}_i^s, \text{ on } \Gamma_t^s, \tag{7}$$

$$w_i = \hat{w}_i, \text{ on } \Gamma_w^f, \tag{8}$$

$$p = \hat{p}, \text{ on } \Gamma_p^f, \tag{9}$$

where $\boldsymbol{n} = (n_1, n_3)$ is the normal vector to the boundary, and $\hat{u}_i^s$, $\hat{t}_i^s$, $\hat{w}_i$ and $\hat{p}$ are the prescribed solid displacements, tractions, relative fluid displacements and pore pressure on the boundary, respectively.

We introduce the Fourier transform with respect to time and frequency as

$$\widetilde{f}(\omega) = \int_{-\infty}^{+\infty} f(t) e^{-\mathrm{j}\omega t} dt,\ f(t) = \frac{1}{2\pi}\int_{-\infty}^{+\infty} \widetilde{f}(\omega) e^{\mathrm{j}\omega t} d\omega, \tag{10}$$

where $\mathrm{j} = \sqrt{-1}$ is the imaginary unit.

After Fourier transform on Equations (3) and (4), the frequency-domain governing equations in terms of solid displacement and fluid pressure [54] are recast as

$$\mu \widetilde{u}_{i,jj} + (\lambda + \mu)\widetilde{u}_{j,ji} + \rho_g \omega^2 \widetilde{u}_i - \alpha_g \widetilde{p}_{,i} = 0, \tag{11}$$

$$\widetilde{p}_{,jj} + \beta_2 \omega^2 \widetilde{p} - \beta_3 \widetilde{u}_{j,j} = 0, \tag{12}$$

where $\rho_g = \rho - \beta_4 \rho_f$, $\alpha_g = \alpha - \beta_4$, $\beta_1 = M/\left[m\omega^2 - \mathrm{j}\omega(\eta/k)\widetilde{K}(\omega)\right]$, $\beta_2 = 1/(\beta_1 \omega^2)$, $\beta_4 = \rho_f \omega^2 \beta_1 / M$; $\beta_3 = \rho_f \omega^2 - \alpha\left[m\omega^2 - \mathrm{j}\omega(\eta/k)\widetilde{K}(\omega)\right]$, $\widetilde{K}(\omega)$ is the Fourier transform of $K(t)$, and "~" denotes the representation in the frequency-domain.

3. Singular Boundary Method in Frequency-Domain

In this section, the SBM formulation is established for the frequency-domain governing equations. The SBM evaluates the frequency-domain solution with a linear combination of fundamental solutions in terms of the source points as [55]

$$\widetilde{u}_i^s(\boldsymbol{x}_m) = \sum_{n=1}^{N} \beta_{1n} \widetilde{u}_{i1}^s(\boldsymbol{x}_m, \boldsymbol{s}_n) + \sum_{n=1}^{N} \beta_{3n} \widetilde{u}_{i3}^s(\boldsymbol{x}_m, \boldsymbol{s}_n) + \sum_{n=1}^{N} \beta_{4n} \widetilde{u}_{i4}^s(\boldsymbol{x}_m, \boldsymbol{s}_n),\ i = 1, 3, \tag{13}$$

$$\widetilde{p}(\boldsymbol{x}_m) = \sum_{n=1}^{N} \beta_{1n} \widetilde{p}_1(\boldsymbol{x}_m, \boldsymbol{s}_n) + \sum_{n=1}^{N} \beta_{3n} \widetilde{p}_3(\boldsymbol{x}_m, \boldsymbol{s}_n) + \sum_{n=1}^{N} \beta_{4n} \widetilde{p}_4(\boldsymbol{x}_m, \boldsymbol{s}_n), \tag{14}$$

$$\widetilde{t}_i^s(\boldsymbol{x}_m) = \sum_{n=1}^{N} \beta_{1n} \widetilde{t}_{i1}^s(\boldsymbol{x}_m, \boldsymbol{s}_n) + \sum_{n=1}^{N} \beta_{3n} \widetilde{t}_{i3}^s(\boldsymbol{x}_m, \boldsymbol{s}_n) + \sum_{n=1}^{N} \beta_{4n} \widetilde{t}_{i4}^s(\boldsymbol{x}_m, \boldsymbol{s}_n),\ i = 1, 3, \tag{15}$$

$$\widetilde{q}_{\mathbf{n}}(\boldsymbol{x}_m) = \sum_{n=1}^{N} \beta_{1n} \widetilde{q}_1(\boldsymbol{x}_m, \boldsymbol{s}_n) + \sum_{n=1}^{N} \beta_{3n} \widetilde{q}_3(\boldsymbol{x}_m, \boldsymbol{s}_n) + \sum_{n=1}^{N} \beta_{4n} \widetilde{q}_4(\boldsymbol{x}_m, \boldsymbol{s}_n). \tag{16}$$

where $\boldsymbol{x}_m, \boldsymbol{s}_n$ are the mth field point and nth source point; N is the total number of boundary source points; $\{\beta_{kn}\}_{n=1}^{N}(k=1,3,4)$ are the coefficients to be determined; and $\widetilde{u}_{ik}^s$, $\widetilde{t}_{ik}^s$, $\widetilde{p}_k$ and $\widetilde{q}_k$ $(i=1,3,\ k=1,3,4)$ are the fundamental solutions of solid displacements, traction, pore pressure and flux, which are given as

$$\widetilde{u}_{ik}^s = A\delta_{ik} - Br_{,i}r_{,k},\ \widetilde{u}_{i4}^s = Dr_{,i},\ i,k=1,3, \tag{17}$$

$$\begin{aligned}\widetilde{t}_{ik}^s &= \lambda\left[A' - B' - \tfrac{B}{r}\right]r_{,k}n_i + \mu\left[\left(A' - \tfrac{B}{r}\right)(r_{,n}\delta_{ik} + r_{,i}n_k)\right.\\ &\left. -\tfrac{2B}{r}r_{,k}n_i + 2\left(-B' + \tfrac{2B}{r}\right)r_{,i}r_{,k}r_{,n}\right],\ i,k=1,3,\\ \widetilde{t}_{i4}^s &= \left[(\lambda+2\mu)\tfrac{D}{r} + \lambda D'\right]n_i + 2\mu\left(-\tfrac{D}{r} + D'\right)r_{,i}r_{,n},\ i=1,3,\end{aligned} \tag{18}$$

$$\widetilde{p}_k = Cr_{,k},\ \widetilde{p}_4 = \frac{1}{2\pi}\sum_{d=1,2} r_d h_d K_0(z_d),\ k=1,3, \tag{19}$$

$$\widetilde{q}_k = \begin{cases} \frac{-\alpha_g}{\beta_3}\left[\frac{C}{r}n_k + \left(C' - \frac{C}{r}\right)r_{,k}r_{,n}\right],\ k=1,3,\\ \frac{\mathrm{j}\alpha_g r_{,n}}{2\pi\beta_3}\sum\limits_{d=1,2} r_d h_d k_d K_1(z_d),\ k=4, \end{cases} \tag{20}$$

where

$$A = \frac{1}{2\pi}\left[-\sum_{d=1,2} g_d\frac{K_1(z_d)}{z_d} + g_3\left(K_0(z_3) + \frac{K_1(z_3)}{z_3}\right)\right],\ C = \frac{\mathrm{j}}{2\pi}\left[\sum_{d=1,2}\frac{r_d g_d}{k_d}K_1(z_d)\right]$$

$$B = \frac{1}{2\pi}\left[-\sum_{d=1,2} g_d K_2(z_d) + g_3 K_2(z_3)\right],\ D = \frac{-\mathrm{j}}{2\pi}\sum_{d=1,2} k_d h_d K_1(z_d) z_3 = \mathrm{j}k_3 r$$

$$z_d = \mathrm{j}k_d r,\ r_d = \frac{\omega^2\rho_g - (\lambda+2\mu)k_d^2}{\alpha_g}(d=1,2),\ g_1 = \frac{\beta_3 - r_2}{(\lambda+2\mu)(r_1 - r_2)},$$

$$g_2 = \frac{\beta_3 - r_1}{(\lambda+2\mu)(r_2 - r_1)},\ g_3 = \frac{1}{\mu},\ h_1 = -\frac{\beta_3}{\alpha_g(r_1 - r_2)},\ h_2 = -\frac{\beta_3}{\alpha_g(r_2 - r_1)}$$

in which $r = \sqrt{(x_1 - y_1)^2 + (x_3 - y_3)^2}$ is the distance between field point $\boldsymbol{x} = (x_1, x_3)$ and source point $\boldsymbol{y} = (y_1, y_3)$. K_n is the modified Bessel function of the second kind of order n, and k_d is

$$k_1 = \sqrt{\frac{\beta_2\omega^2}{2} + \frac{\rho_g\omega^2 - \alpha_g\beta_3 + \sqrt{H}}{2(\lambda+2\mu)}},\ k_2 = \sqrt{\frac{\beta_2\omega^2}{2} + \frac{\rho_g\omega^2 - \alpha_g\beta_3 - \sqrt{H}}{2(\lambda+2\mu)}},\ k_3 = \sqrt{\omega^2\rho_g/\mu}$$

where

$$H = \left(\lambda\beta_2\omega^2 - \alpha_g\beta_3 + \rho_g\omega^2\right)^2 + 4(\lambda+\mu)\beta_2\omega^4(\mu\beta_2 - \rho_g) - 4\mu\alpha_g\beta_2\beta_3\omega^2$$

The derivation of the fundamental solutions is detailed in Appendix A.

With the fundamental solutions, Equations (13)–(16) are forced to satisfy the boundary conditions for the determination of the unknown coefficients. Then the boundary conditions with Equations (13)–(16) are formulated as

$$\widetilde{u}_i^s(\boldsymbol{y}_m) = \sum_{k=1,3,4}\sum_{n\neq m}^{N}\beta_{kn}\widetilde{u}_{ik}^s(\boldsymbol{y}_m, \boldsymbol{y}_n) + \sum_{k=1,3,4}\beta_{km}\widetilde{U}_{ik}^s(\boldsymbol{y}_m, \boldsymbol{y}_m),\ i=1,3, \tag{21}$$

$$\widetilde{t}_i^s(\boldsymbol{y}_m) = \sum_{k=1,3,4}\sum_{n\neq m}^{N}\beta_{kn}\widetilde{t}_{ik}^s(\boldsymbol{y}_m, \boldsymbol{y}_n) + \sum_{k=1,3,4}^{3}\beta_{km}\widetilde{T}_{ik}^s(\boldsymbol{y}_m, \boldsymbol{y}_m),\ i=1,3, \tag{22}$$

$$\widetilde{p}(\boldsymbol{y}_m) = \sum_{k=1,3,4} \sum_{n\neq m}^{N} \beta_{kn} \widetilde{p}_k(\boldsymbol{y}_m, \boldsymbol{y}_n) + \sum_{k=1,3,4} \beta_{km} \widetilde{P}_k(\boldsymbol{y}_m, \boldsymbol{y}_m), \tag{23}$$

$$\widetilde{q}_{\mathbf{n}}(\boldsymbol{y}_m) = \sum_{k=1,3,4} \sum_{n\neq m}^{N} \beta_{kn} \widetilde{q}_k(\boldsymbol{y}_m, \boldsymbol{y}_n) + \sum_{k=1,3,4} \beta_{km} \widetilde{Q}_k(\boldsymbol{y}_m, \boldsymbol{y}_m). \tag{24}$$

The singular terms, namely, $\widetilde{u}^s_{ik}(\boldsymbol{y}_m, \boldsymbol{y}_m)$, $\widetilde{t}^s_{ik}(\boldsymbol{y}_m, \boldsymbol{y}_m)$, $\widetilde{p}_k(\boldsymbol{y}_m, \boldsymbol{y}_m)$ and $\widetilde{q}_k(\boldsymbol{y}_m, \boldsymbol{y}_m)$, are involved when the boundary data points overlaps the source points. To deal with this issue, some numerical or analytical methods are introduced to desingularize these terms. In the SBM, the diagonal terms are called the origin intensity factors (OIFs), as $\widetilde{U}^s_{ik}(\boldsymbol{y}_m, \boldsymbol{y}_m)$, $\widetilde{T}^s_{ik}(\boldsymbol{y}_m, \boldsymbol{y}_m)$, $\widetilde{P}_k(\boldsymbol{y}_m, \boldsymbol{y}_m)$ and $\widetilde{Q}_k(\boldsymbol{y}_m, \boldsymbol{y}_m)$ in Equations (21)–(24). The OIFs for 2D saturated poroelastic problems [20,21,56], as shown in Equations (21)–(24) are calculated as

$$\widetilde{U}^s_{ik}(\boldsymbol{y}_m, \boldsymbol{y}_m) = \begin{cases} [\hat{g}(\boldsymbol{y}_m, \boldsymbol{y}_m)\chi_1 - \chi_2]\delta_{ik} + \chi_3 \Lambda_{ik}, \ i,k = 1,3, \\ 0, \ k = 4, \ i = 1,3, \end{cases} \tag{25}$$

$$\widetilde{T}^s_{ik}(\boldsymbol{y}_m, \boldsymbol{y}_m) = \begin{cases} \hat{t}_{ik}(\boldsymbol{y}_m, \boldsymbol{y}_m), \ i,k = 1,3, \\ [\hat{g}(\boldsymbol{y}_m, \boldsymbol{y}_m)\chi_4 + \chi_5]n_i, \ k = 4, \ i = 1,3, \end{cases} \tag{26}$$

$$\widetilde{P}_k(\boldsymbol{y}_m, \boldsymbol{y}_m) = \begin{cases} 0, \ k = 1,3, \\ \hat{g}(\boldsymbol{y}_m, \boldsymbol{y}_m)\chi_6 + \chi_7, \ k = 4, \end{cases} \tag{27}$$

$$\widetilde{Q}_k(\boldsymbol{y}_m, \boldsymbol{y}_m) = \begin{cases} [\hat{g}(\boldsymbol{y}_m, \boldsymbol{y}_m)\chi_8 + \chi_9]n_k, \ k = 1,3, \\ \hat{q}(\boldsymbol{y}_m, \boldsymbol{y}_m)\chi_{10}, \ k = 4, \end{cases} \tag{28}$$

where $\chi_1, \ldots, \chi_{10}$ are provided in Appendix B; $\Lambda_{ik} = \lim\limits_{x\to y, x\in\Gamma} r_{,i} r_{,k} = \frac{\tau_i \tau_k}{\tau_1^2 + \tau_3^2}$, $\boldsymbol{\tau} = (\tau_1, \tau_3)$ is the tangent vector of point $\boldsymbol{x}$ on the boundary, $\hat{g}(\boldsymbol{y}_m, \boldsymbol{y}_m)$ and $\hat{q}(\boldsymbol{y}_m, \boldsymbol{y}_m)$ are the OIFs for the fundamental solution of the Laplace operator for Dirichlet and Neumann boundary conditions, and $\hat{t}_{ik}(\boldsymbol{y}_m, \boldsymbol{y}_m)$ is the OIF for the fundamental solution of the traction boundary condition. These terms are computed as

$$\hat{g}(\boldsymbol{y}_m, \boldsymbol{y}_m) = -\frac{1}{2\pi} \ln\left(\frac{l_m}{2\pi}\right), \ \hat{q}(\boldsymbol{y}_m, \boldsymbol{y}_m) = -\frac{1}{2l_m}, \ \hat{t}_{ij}(\boldsymbol{y}_m, \boldsymbol{y}_m) = -\frac{\delta_{ij}}{2l_m} \tag{29}$$

where l_m is a half-length of the arc between source points $\boldsymbol{y}_{m+1}$ and $\boldsymbol{y}_{m-1}$.

Finally after obtaining the coefficients, the frequency-domain solutions of the variables within the domain can be evaluated via Equations (13)–(16).

4. Exponential Window Method

The frequency-domain solutions can be converted to the transient solutions via the inverse Fourier transform, which is accelerated by the fast Fourier transformation (FFT) [47,57]. It should be noted that the time responses decay slowly in lightly damped systems, and even never decay in undamped systems. In these two cases, the FFT is inefficient. Thus, a powerful numerical technique, the exponential window method (EWM) [58], is introduced. In the EWM, artificial damping is created to produce the desired attenuation, and the artificial damping is removed by scaling back in the final. The detail of the EWM is summarized as follows:

(1) Determine the total calculation time T and the number of sampling frequencies N_ω, then to determine the angular frequency resolution $\Delta\omega = 2\pi/T$ with $\Delta t = T/N_\omega$;

(2) Determine the shifting constant according to the numerical experiments and experience as

$$\vartheta = \frac{\kappa \ln 10}{T}, \tag{30}$$

where κ denote the damping coefficient, and $2 \leq \kappa \leq 3$ is recommended;

(3) Construct a desired damping system with scaling the variables $\xi(\boldsymbol{x},t)$ (u_i^s, σ_{ik}^s, w_i and p) with the scaling function $e^{-\vartheta t}$ as $\xi_{ew}(\boldsymbol{x},t)=\xi(\boldsymbol{x},t)e^{-\vartheta t}$. Bring new variables ξ_{ew} into the governing equations, and a novel frequency-domain boundary value problem Equations (6) and (7) with $\overline{\omega}=\omega-\mathrm{j}\vartheta$ is obtained.

(4) Simultaneously, the boundary condition $P(\boldsymbol{x},t)$ is scaled into $P_{ew}(\boldsymbol{x},t)=P(\boldsymbol{x},t)e^{-\vartheta t}$, and the frequency-domain boundary condition can be obtained via discretized Fourier transform

$$\hat{P}_{ew}(\boldsymbol{x},\overline{\omega}_k)=\frac{1}{N_\omega}\sum_{n=0}^{N_\omega-1}P_{ew}(\boldsymbol{x},n\Delta t)e^{-2\pi\mathrm{j}nk/N_\omega}=\frac{1}{N_\omega}\sum_{n=0}^{N_\omega-1}e^{-\vartheta n\Delta t}P(\boldsymbol{x},n\Delta t)e^{-2\pi\mathrm{j}nk/N_\omega}, \tag{31}$$

where $\overline{\omega}_k=k\Delta\omega-\mathrm{j}\vartheta(k=0,1,\ldots,N_\omega-1)$.

(5) Perform the SBM to evaluate the solutions of the frequency-domain problems $R_{ew}^*(\overline{\omega}_k)$ at the frequencies $\overline{\omega}_k=k\Delta\omega-\mathrm{j}\vartheta(k=0,1,\ldots,N_\omega/2)$. The remaining of results can be obtained through conjugate symmetric property as

$$R_{ew}^*(\overline{\omega}_k)=\mathrm{conj}(R_{ew}^*(\overline{\omega}_{N_\omega-k})),\ k=N_\omega/2+1,\ldots,N_\omega-1. \tag{32}$$

(6) Perform the IFFT with the inverse DFT with Hanning window function W_k, and obtain the time-domain solutions as

$$R_{ew}(n\Delta t)=\sum_{k=1}^{N_\omega-1}W_kR_{ew}^*(\overline{\omega}_k)e^{2\pi\mathrm{j}nk/N_\omega}, \tag{33}$$

The Hanning window function $W_k=0.5[1+\cos(2\pi k/N_\omega)]$ is used to alleviate the Gibbs oscillations.

(7) Descale the time-domain solutions and obtain the solutions of the original problems as

$$R(n\Delta t)=e^{\vartheta n\Delta t}R_{ew}(n\Delta t). \tag{34}$$

5. Numerical Examples

In this section, three numerical examples are used to verify the accuracy and effectiveness of the proposed method for the transient dynamic response of two-dimensional saturated soil. The accuracy of the SBM-EWM is evaluated by the absolute error of variable ξ versus time at point $\boldsymbol{x}$ as

$$AE(\xi)=\left|\overline{\xi}\left(\frac{kT}{N_\omega},\boldsymbol{x}\right)-\xi\left(\frac{kT}{N_\omega},\boldsymbol{x}\right)\right|, \tag{35}$$

where $\overline{\xi}$ represents the exact solution, ξ denotes the numerical result obtained by the SBM.

Unless otherwise specified, the parameters of the saturated soil are set as $\lambda=4.0\times10^7$ Pa, $\mu=2.0\times10^7$ Pa, $\rho_s=2500$ kg/m^3, $\rho_f=1.0\times10^3$ kg/m^3, $a_\infty=3$, $\alpha=0.95$, $M=4.0\times10^8$ Pa, $\phi=0.3$, $\eta=1.0\times10^{-3}$ Pa·s, $k=1.0\times10^{-12}$ m^2. All calculations of this paper are fulfilled on a desktop with an Intel Core (TM) I7-6500U at 2.50 GHz on a 64-bit Windows server with a total of 12GB DDR4 memory. The SBM is implemented via MATLAB software.

5.1. Verification of the Proposed SBM-EWM Method

In the section, a saturated poroelastic column problem (Figure 1) is considered. A uniform normal load on the upper boundary and the rest boundaries is sliding:

$$\begin{cases}\mathrm{t_n^s}=-\mathrm{H(t)N/m^2},\mathrm{t_\tau^s}=0\mathrm{N/m^2},\mathrm{p}=0\mathrm{Pa},\ \text{on the top boundary},\\ \mathrm{u_n^s}=0\mathrm{m},\mathrm{t_\tau^s}=0\mathrm{N/m^2},\mathrm{w_n}=0\mathrm{m},\ \text{on the other boundaries},\end{cases} \tag{36}$$

where $H(t)$ is the Heaviside step function.

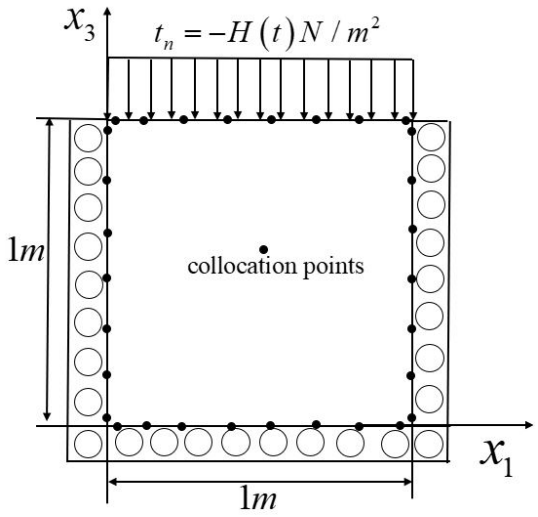

Figure 1. Computational model of saturated column.

Firstly, the transient problem is transformed into the frequency domain. The frequency-domain exact solution for the problem can be constructed as

$$\begin{aligned} \widetilde{u}_3^s &= a_1 \mathrm{j}k_1 e^{\mathrm{j}k_1(x_3-h)} + a_2 \mathrm{j}k_2 e^{\mathrm{j}k_2(x_3-h)} - a_3 \mathrm{j}k_1 e^{-\mathrm{j}k_1 x_3} - a_4 \mathrm{j}k_2 e^{-\mathrm{j}k_2 x_3}, \\ \widetilde{p} &= a_1 r_1 e^{\mathrm{j}k_1(x_3-h)} + a_2 r_2 e^{\mathrm{j}k_2(x_3-h)} + a_3 r_1 e^{-\mathrm{j}k_1 x_3} + a_4 r_2 e^{-\mathrm{j}k_2 x_3}, \end{aligned} \tag{37}$$

in which h = 1 m, and the unknown coefficients a_1, a_2, a_3 and a_4 can be derived from

$$\begin{bmatrix} -k_1^2 & -k_2^2 & -k_1^2 e^{-\mathrm{j}k_1 h} & -k_2^2 e^{-\mathrm{j}k_2 h} \\ r_1 & r_2 & r_1 e^{-\mathrm{j}k_1 h} & r_2 e^{-\mathrm{j}k_2 h} \\ \mathrm{j}k_1 e^{-\mathrm{j}k_1 h} & \mathrm{j}k_2 e^{-\mathrm{j}k_2 h} & -\mathrm{j}k_1 & -\mathrm{j}k_2 \\ \mathrm{j}k_1\left(r_1 - \omega^2\rho_f\right)e^{-\mathrm{j}k_1 h} & \mathrm{j}k_2\left(r_2 - \omega^2\rho_f\right)e^{-\mathrm{j}k_2 h} & \mathrm{j}k_1\left(r_1 - \omega^2\rho_f\right) & \mathrm{j}k_2\left(r_2 - \omega^2\rho_f\right) \end{bmatrix} \begin{bmatrix} a_1 \\ a_2 \\ a_3 \\ a_4 \end{bmatrix} = \begin{bmatrix} \frac{-1}{\lambda+2\mu} \\ 0 \\ 0 \\ 0 \end{bmatrix}$$

Then the transient exact solution is retrieved via the EWM.

The SBM discretizes the boundary into 400 boundary nodes. The EWM-SBM is employed for the numerical solutions in a duration of T = 18 ms. In the EWM, N_ω and κ are set as 128 and 3.

In Figure 2, some numerical results are picked up to show the accuracy of the present method, including u_3^s at (0.5, 0.8), p at (0.5, 0.5), w_3 at (0.5, 0.7) and σ_{33}^s at (0.5, 0.3). It is shown that the numerical results are in good agreement with the exact solutions. Nevertheless, the results without the Hanning window function drastically oscillate in the end of the duration, which is called Gibbs oscillations. The problem is ameliorated by the Hanning window function. The application of the Hanning window functions does not bring much time. For example, in Figure 2a, the SBM-EWM without and with the Hanning window functions, respectively, take 57.08 s and 56.48 s. As a consequence, it is essential to employ the window function in the EWM-SBM.

It is obvious that the selection of the parameters N_ω, κ has an influence on the accuracy and the stability of the solutions. In the following, the influence is studied.

N_ω is the number of the sample frequencies. More sample frequencies enhance the accuracy of the results but in the meantime bring more operation counts. If the sample frequencies are not enough, the numerical methods may yield inaccurate results. Figure 3 shows the effect of N_ω on the numerical methods via σ_{33}^s at (0.5, 0.8) and p at (0.5, 0.5). In this figure, the number of boundary points is 400 and κ = 2.7. As the number of sampling frequencies increases, the numerical solutions converge to the exact solutions. The solution with N_ω = 64 deviates from the exact solutions most in comparison with N_ω = 128 and 256. However, the case with N_ω = 256 takes 111.7 s in total, which is nearly two times that

of the case with N_ω = 128, which consumes 59.3 s. Overall, N_ω = 128 is considered in the following numerical experiments.

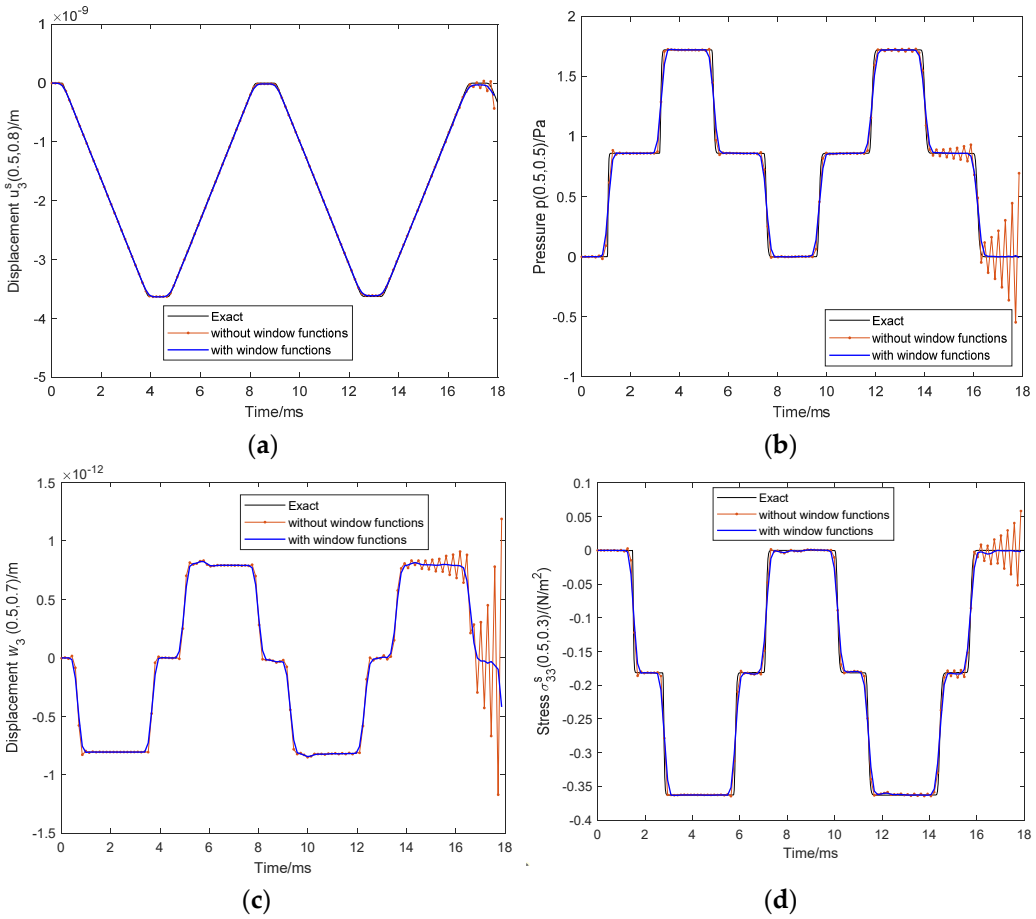

Figure 2. Time history of (**a**) u_3^s at (0.5, 0.8), (**b**) p at (0.5, 0.5), (**c**) w_3 at (0.5, 0.7), (**d**) σ_{33}^s at (0.5, 0.3).

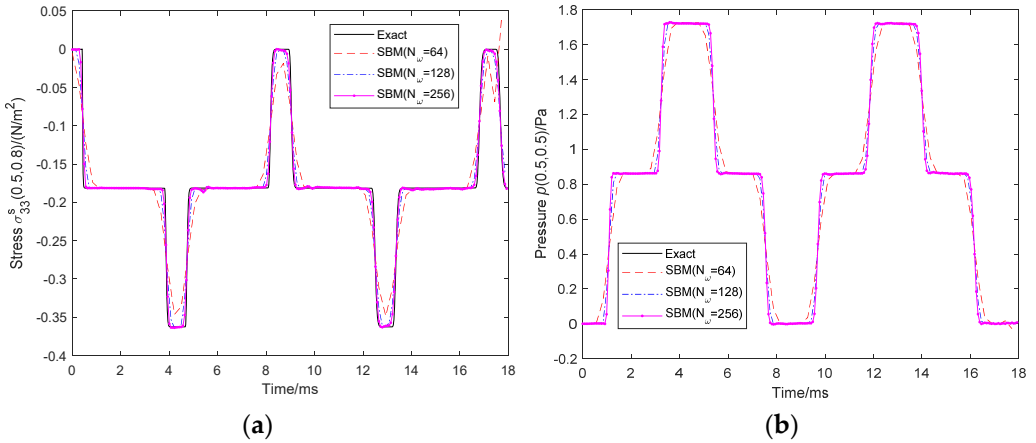

Figure 3. Time history of (**a**) σ_{33}^s at (0.5, 0.8) and (**b**) p at (0.5, 0.5) with respect to the number of sampling frequencies N_ω.

κ is the damping coefficient to determine the artificial damping. A numerical investigation on the κ is given in Figure 4 via the absolute error of u_3^s at (0.5, 0.5) under different damping coefficients. κ = 1.5, 2, 2.5, 3 and 3.5 are selected. The method with κ = 1.5 results in the worst solutions. The reason lies in that more sampling frequencies are required in

lightly damped systems. In Figure 4, the results with κ = 2, 2.5, 3 and 3.5 are acceptable. Nevertheless, an arbitrary large damping coefficient may lead to loss of numerical precision. As a trade-off, the κ = 2.5 is applied in the subsequent examples.

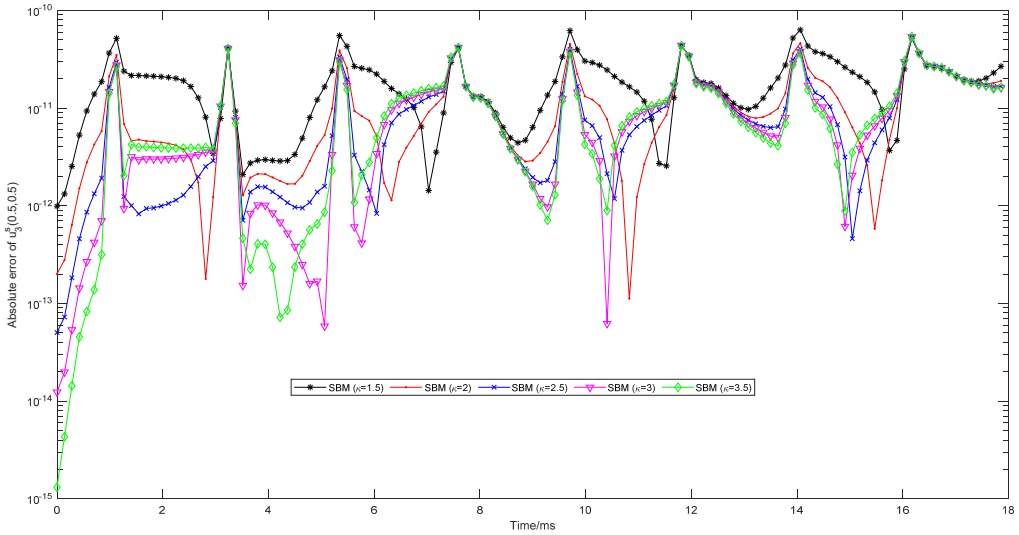

Figure 4. Time history of absolute error of u_3^s at point (0.5, 0.5) under different κ.

In general, the numerical transient results are limited to a short time duration because the results deteriorate if the calculation duration is too long. In this study, the long time behavior of the present method is investigated. In this case, T = 140 ms and N_ω = 1024. Figure 5 plots the history of u_3^s at (0.5, 0.8) and p at (0.5, 0.5). In the entire calculation time, no obvious differences can be observed between the SBM-EWM and exact solutions, which verifies the accuracy and stability of the SBM-EWM in the long-term dynamic simulation.

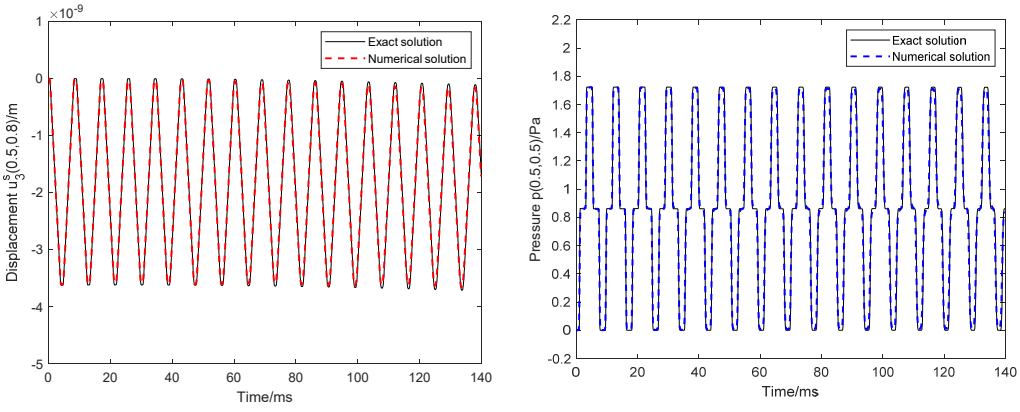

(**a**) (**b**)

Figure 5. A long time dynamic response of saturated column (**a**) u_3^s at (0.5, 0.8) and (**b**) p at (0.5, 0.5).

5.2. A Half-Space Problem Subjected to a Transient Load

In the section, a saturated poroelastic half-space subjected to transient loads on the ground is shown in Figure 6. Thus, the saturated poroelastic half-space is subjected to the boundary condition expressed as

$$\begin{cases} t_3^s = -H(t)\mathrm{N/m^2}, t_1^s = 0\mathrm{N/m^2}, p = 0\mathrm{Pa},\ x_1 \in [-1,1], x_3 = 0, \\ t_3^s = 0\mathrm{N/m^2}, t_1^s = 0\mathrm{N/m^2}, p = 0\mathrm{Pa\ rest} \end{cases}$$

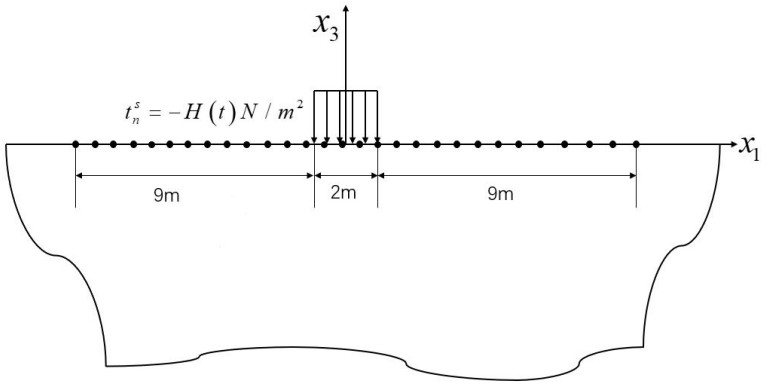

Figure 6. The sketch of the semi-infinite domain.

The boundary is discretized into 500 points. The parameters N_ω, κ are respectively 128 and 2.5 for the SBM. The analytical solution of this problem in frequency-domain is derived by Ba [59]. Then the transient analytical solution is obtained by the EWM with $N_\omega = 256$ and $\kappa = 2.5$. The mesh plots of the analytical solutions and SBM solutions are displayed in Figures 7 and 8. The solutions at different times at different depths are plotted. Good agreement indicates that the SBM is successfully applied to the half-space transient problem.

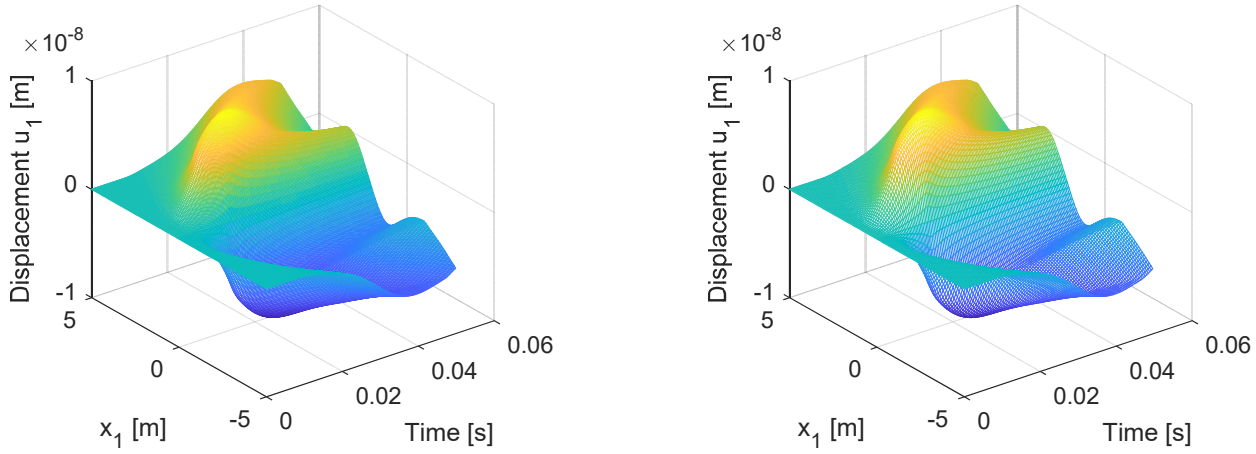

Figure 7. Time history of u_1 at $x_3 = -1$ generated by the analytical solution (**left**) and the SBM-EWM (**right**).

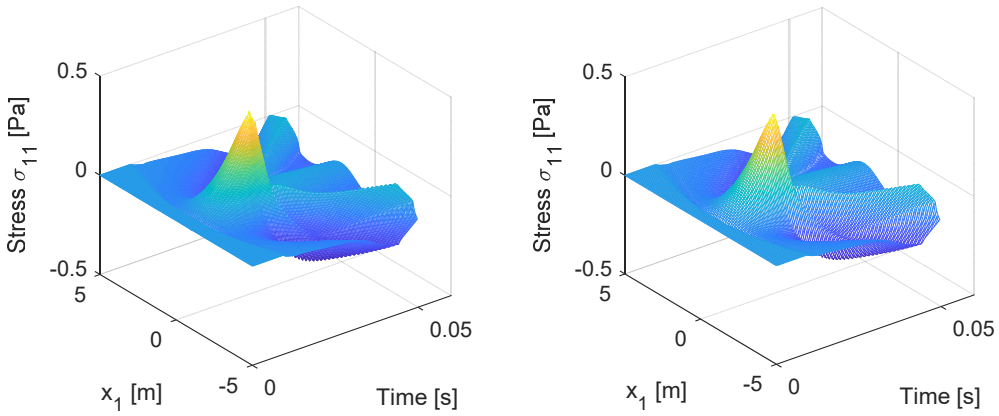

Figure 8. Time history of σ_{11} at $x_3 = -2$ generated by the analytical solution (**left**) and the SBM-EWM (**right**).

Furthermore, the MFS is introduced for comparison with the SBM in Figure 9. All the parameters for the MFS and SBM are the same as the above. The MFS avoids the origin singularity via the artificial boundary outside the computational domain. d is the distance between the artificial boundary and physical boundary. To obtain stable solutions, the MATLAB built-in function pinv is used to solve the linear system of the MFS. As shown in the figure, the MFS and SBM could obtain acceptable solutions. Nevertheless, the results of the MFS are influenced by the location of the artificial boundary. Only the MFS with $d = 0.1$ converges to the analytical solutions. Otherwise, because of the application of pinv, the MFS takes 357.34 s for the whole process, while the SBM takes 92.96 s. It can be observed that the MFS takes a much longer time than the SBM.

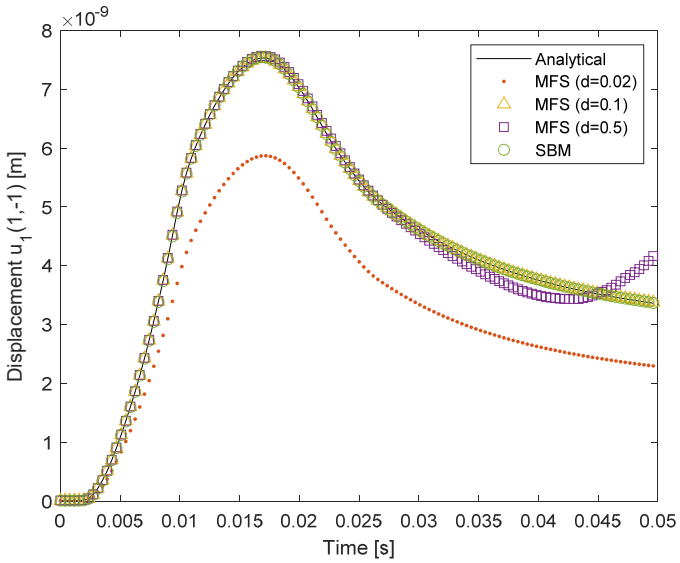

Figure 9. Numerical comparison between the MFS and SBM.

5.3. A Tunnel Embedded in a Saturated Poroelastic Half-Space

In this example, a model of a semi-circular tunnel embedded in a saturated poroelastic half-space in Figure 10 is considered. The radius of the tunnel is $R = 3$ m and the depth of invert of the tunnel is $H = 6$ m. A triangularly distributed transient load is imposed at the invert of the tunnel. The ground and the surface of the tunnel are set as permeable. Thus, the boundary conditions are expressed as

$$\begin{cases} t_3^s = ((|x| - 3)P(t))\mathrm{N/m^2},\ t_1^s = 0\mathrm{N/m^2}, p = 0\mathrm{Pa},\ x_1 \in [-3,\ 3],\ x_3 = -6 \\ t_3^s = 0\mathrm{N/m^2}, t_1^s = 0\mathrm{N/m^2}, p = 0\mathrm{Pa},\ \text{otherwise} \end{cases},$$

where

$$P(t) = \begin{cases} 100t\ 0 \le t \le 0.01 \\ 1\ \ 0.01 < t \le 0.03 \\ 4 - 100t\ 0.03 < t \le 0.04 \\ 0\ \text{otherwise} \end{cases}$$

In this case, no analytical solution is available. Thus, the accuracy of the SBM-EWM is presented with different parameters. The total time of tunnel transient response T is 90 ms, and the damping coefficient $\boldsymbol{\kappa}$ is 2.5. Figure 11 gives σ_{33}^s at $(-2, -7)$ and p at $(1, -7)$ calculated by the SBM-EWM with different numbers of sampling frequencies N_ω (128, 256) and numbers of boundary points N (471, 786). It is observed that the SBM-EWM with different parameters obtains identical results.

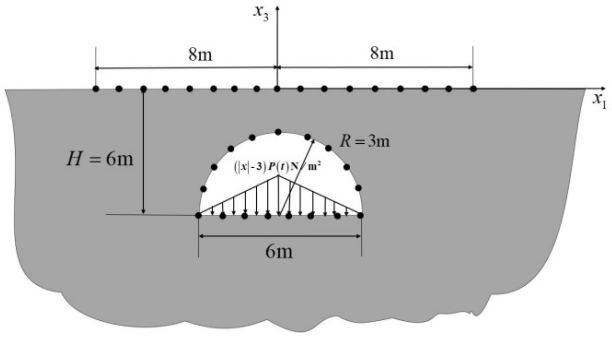

Figure 10. Schematic sketch of the semi-infinite domain tunnel.

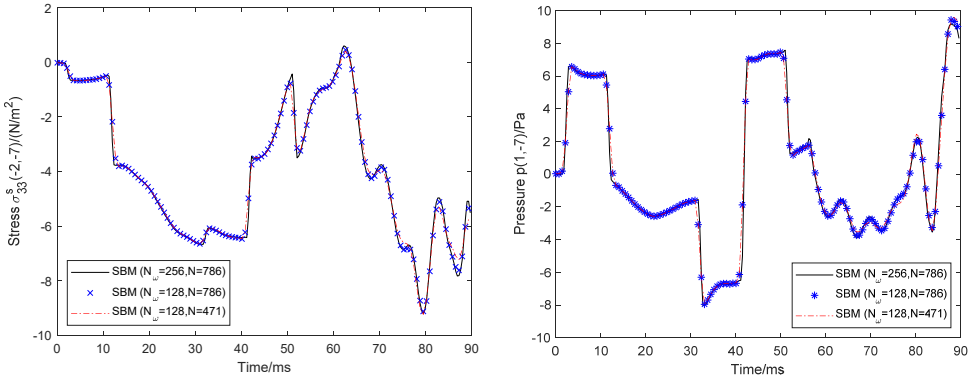

(**a**) (**b**)

Figure 11. Time history of (**a**) σ_{33}^s at $(-2, -7)$ and (**b**) p at $(1, -7)$ under different sampling numbers and boundary points.

To further investigate the numerical results, the time history of the distribution of u_3^s and p of the domain $(x_1, x_3) \in [-10, 10] \times [-20, 0]$ are plotted in Figures 12 and 13 to observe the wave propagation in the entire time. In all results, the dynamic response is symmetric, which is reasonable according to the symmetry loads. In both figures, it can be seen that the wave is caused by loads at the invert of the tunnel. Then it propagates outward in different directions and around the tunnel to the ground. Theoretically speaking, the whole propagation process complies with the law of wave propagation in solids.

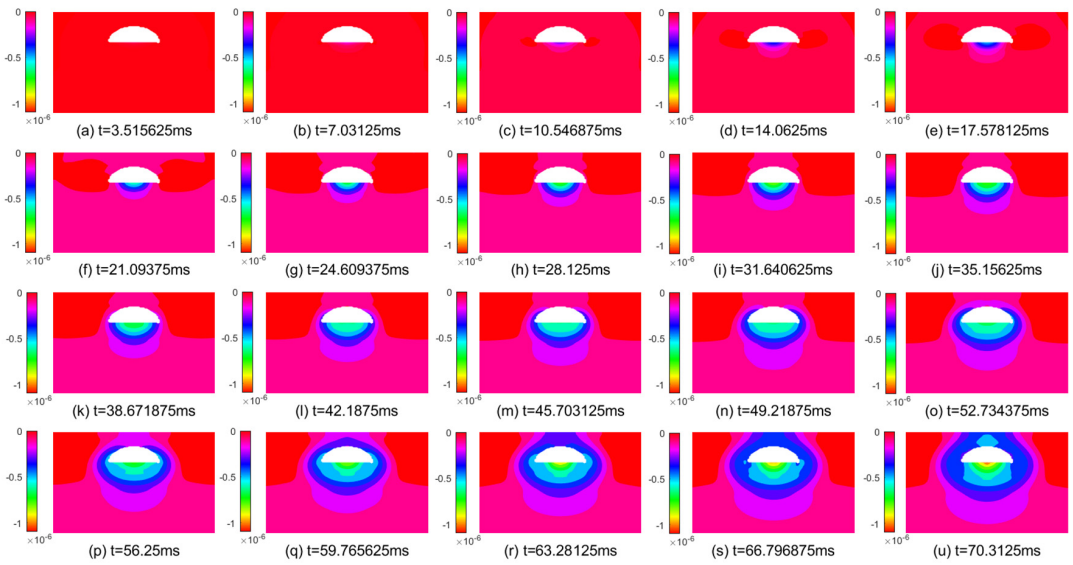

Figure 12. Distribution of u_3^s with of domain $(x_1, x_3) \in [-10, 10] \times [-20, 0]$ at different times.

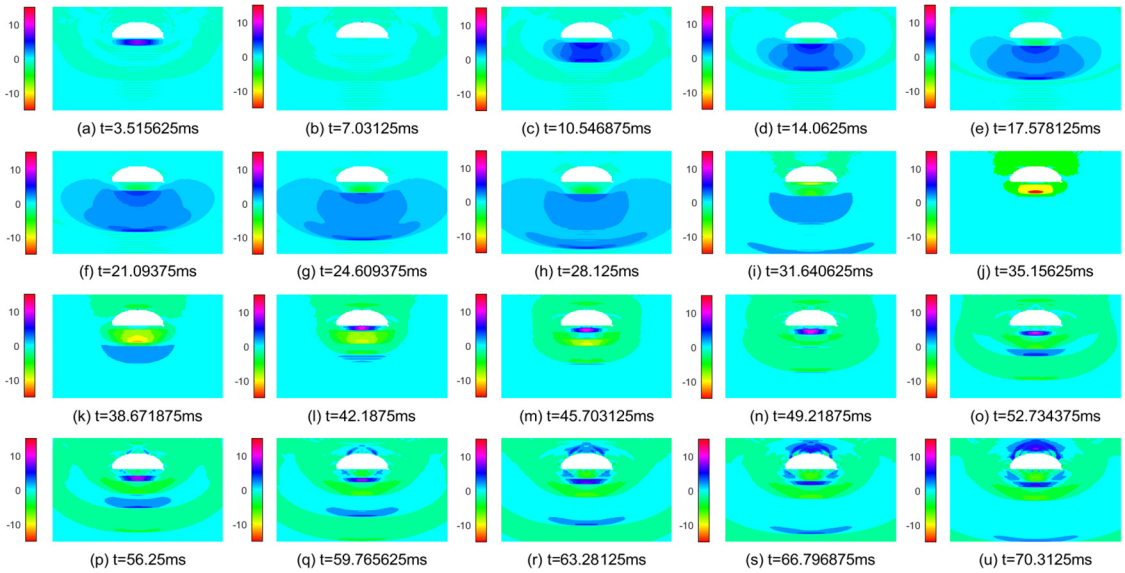

Figure 13. Distribution of p with of domain $(x_1, x_3) \in [-10, 10] \times [-20, 0]$ at different times.

6. Conclusions

In this paper, a novel boundary-only meshless approach is developed to simulate transient dynamic response in the saturated soil. In this method, the SBM is employed to solve the frequency-domain governing equations, while the EWM transforms the frequency-domain solutions into time-domain solutions. In the SBM, the solutions are approximated via the fundamental solutions in terms of boundary points. The boundary-only property makes the SBM very suitable in solving semi-infinite domain problems. The fundamental solutions are derived via the wave decomposition method and eigenanalysis, and their source singularities are removed by the OIFs. The EWM is boasted as an effective inverse Fourier transform method, which incorporates exponential artificial damping into the FFT to enhance its numerical efficiency. The Hanning window function is used to smooth the Gibbs oscillation as the computation period increases. The influence of the parameters in the EWM was investigated in the first numerical experiment. All numerical results validate that the present SBM-EWM is accurate and effective to solve the transient soil dynamic response. Nevertheless, the SBM-EWM is only applicable when the fundamental solutions exist because the fundamental solutions are the kernel function of the SBM.

Author Contributions: Conceptualization, D.L., X.W. and L.S.; Formal analysis, X.W., C.L. and L.S.; Funding acquisition, X.W.; Investigation, C.L. and L.S.; Methodology, D.L., X.W. and L.S.; Software, D.L., X.W. and L.S.; Validation, D.L., X.W., C.L., C.H. and X.C.; Writing—original draft, X.W., C.L. and C.H.; Writing—review and editing, X.C. and L.S. All authors have read and agreed to the published version of the manuscript.

Funding: This work is supported by the National Natural Science Foundation of China (Grant No. 12102135, 51978265, 11602114, 11662003) and Double Thousand Talents Project from Jiangxi Province, The Natural Science Foundation of Jiangxi Province of China (Grant No. 20202BABL201014).

Institutional Review Board Statement: Not applicable.

Informed Consent Statement: Not applicable.

Data Availability Statement: Not applicable.

Acknowledgments: This work is supported by the National Natural Science Foundation of China (Grant No. 12102135, 51978265, 11602114, 11662003) and Double Thousand Talents Project from Jiangxi Province, The Natural Science Foundation of Jiangxi Province of China (Grant No. 20202BABL 201014, 20202ACB211002).

Conflicts of Interest: The authors declare no conflict of interest.

Appendix A. Detailed Derivations of the 2D Fundamental Solutions

The fundamental solution is one of most important parts for the boundary-only methods. However, it is not a trivial work to derive the fundamental solutions for coupled governing equations. This section decouples the governing equations into several simpler scalar governing equations with known fundamental solutions, and then coupled these fundamental solutions with the eigenanalysis.

(1) Solid loads

The singular loads are applied to the solid phase as $\boldsymbol{F}^s = -\delta(\boldsymbol{x}-\boldsymbol{y})\boldsymbol{e}^k (k = 1,3)$ where $\boldsymbol{e}^1$ and $\boldsymbol{e}^3$ are the unit vectors along x_1 and x_3 direction. The variables in governing Equations (11) and (12) are decomposed into underdetermined potentials A_L, A_T and A_P as

$$\widetilde{\boldsymbol{u}}^s = \nabla\nabla\cdot\left(A_L\boldsymbol{e}^k\right) - \nabla\times\nabla\times\left(A_T\boldsymbol{e}^k\right), \tag{A1}$$

$$\widetilde{p} = \nabla\cdot\left(A_P\boldsymbol{e}^k\right), \tag{A2}$$

The Laplace operator can be decomposed into

$$\Delta\left(\tau\boldsymbol{e}^k\right) = \nabla\nabla\cdot\left(\tau\boldsymbol{e}^k\right) - \nabla\times\nabla\times\left(\tau\boldsymbol{e}^k\right) = -\delta(\boldsymbol{y}-\boldsymbol{x})\boldsymbol{e}^k, \tag{A3}$$

where τ is the fundamental solutions for the Laplace operator.

With Equations (A1) and (A2), we decouple the governing Equations (11) and (12) as

$$(\lambda+2\mu)\nabla^2 A_L + \omega^2\rho_g A_L - \alpha_g A_P = \tau, \tag{A4}$$

$$\mu\nabla^2 A_T + \omega^2\rho_g A_T = \tau, \tag{A5}$$

$$\nabla^2 A_P + \omega^2\beta_2 A_P - \beta_3\nabla^2 A_L = 0. \tag{A6}$$

Potentials A_T can be obtained from Equation (A5) as

$$A_T = -\frac{g_3}{2\pi k_3^2}(\ln r + K_0(\mathrm{j}k_3 r)). \tag{A7}$$

The other two potentials A_L and A_P are coupled in Equations (A4) and (A6). To solve A_L and A_P, the eigenanalysis is introduced for the matrix system as

$$M_1\nabla^2\begin{bmatrix} A_L \\ A_P \end{bmatrix} + M_2\begin{bmatrix} A_L \\ A_P \end{bmatrix} = \begin{bmatrix} \tau \\ 0 \end{bmatrix}, \tag{A8}$$

where

$$M_1 = \begin{bmatrix} \lambda+2\mu & 0 \\ -\beta_3 & 1 \end{bmatrix},\ M_2 = \begin{bmatrix} \omega^2\rho_g & -\alpha_g \\ 0 & \beta_2\omega^2 \end{bmatrix}$$

Reformulate Equation (A8) as

$$\nabla^2\begin{bmatrix} A_L \\ A_P \end{bmatrix} + M\begin{bmatrix} A_L \\ A_P \end{bmatrix} = \tau M_1^{-1}\begin{bmatrix} 1 \\ 0 \end{bmatrix} = \tau\boldsymbol{g},\ M = M_1^{-1}M_2 \tag{A9}$$

with matrix $\boldsymbol{g}$ written as

$$\boldsymbol{g} = \frac{1}{\lambda+2\mu}\begin{bmatrix} 1 \\ \beta_3 \end{bmatrix} \tag{A10}$$

Search the solutions through the eigenvector basis as

$$\begin{bmatrix} A_L \\ A_P \end{bmatrix} = \phi_1\begin{bmatrix} 1 \\ r_1' \end{bmatrix} + \phi_2\begin{bmatrix} 1 \\ r_2' \end{bmatrix}, \tag{A11}$$

where $\left(1, r_i'\right)^T (i = 1, 2)$ denote the eigenvector of $\boldsymbol{M}$ and r_1', r_2' are given by

$$r_i' = \frac{(\lambda + 2\mu)k_i^2 - \omega^2\rho_g}{-\alpha_g}, \ i = 1, 2, \tag{A12}$$

where $k_i^2 (i = 1, 2)$ are the eigenvalue of $\boldsymbol{M}$ and $k_3^2 = \omega^2\rho_g/\mu$. Then based on Equations (A11), Equation (A9) can be simplified as

$$\nabla^2\phi_i + k_i^2\phi_i = g_i\tau, \tag{A13}$$

where $g_3 = 1/\mu$ and $g_i (i = 1, 2)$ are

$$\boldsymbol{g} = g_1 \begin{bmatrix} 1 \\ r_1' \end{bmatrix} + g_2 \begin{bmatrix} 1 \\ r_2' \end{bmatrix}. \tag{A14}$$

Thus, the solution of Equation (A13) is

$$\phi_i(r) = -\frac{g_i}{2\pi k_i^2}(\ln r + K_0(\mathrm{j}k_i r)), \tag{A15}$$

where K_0 is the modified Bessel function of zero order.

Bringing the potentials into Equations (A1) and (A2), the 2D fundamental solutions are derived as

$$\widetilde{u}_{ik}^s = A\delta_{ik} - Br_{,i}r_{,k}, \ i, k = 1, 3, \tag{A16}$$

$$\widetilde{p}_k = Cr_{,k}, \ k = 1, 3. \tag{A17}$$

where

$$A = \frac{1}{2\pi}\left[-\sum_{d=1,2} g_d \frac{K_1(z_d)}{z_d} + g_3\left(K_0(z_3) + \frac{K_1(z_3)}{z_3}\right)\right]$$

$$C = \frac{\mathrm{j}}{2\pi}\left[\sum_{d=1,2} \frac{r_d g_d}{k_d} K_1(z_d)\right]$$

$$B = \frac{1}{2\pi}\left[-\sum_{d=1,2} g_d K_2(z_d) + g_3 K_2(z_3)\right]$$

$$D = \frac{-\mathrm{j}}{2\pi}\sum_{d=1,2} k_d h_d K_1(z_d), \ z_3 = \mathrm{j}k_3 r, \ z_d = \mathrm{j}k_d r$$

$$r_d = \frac{\omega^2\rho_g - (\lambda + 2\mu)k_d^2}{\alpha_g} (d = 1, 2), \ g_1 = \frac{\beta_3 - r_2}{(\lambda + 2\mu)(r_1 - r_2)},$$

$$g_2 = \frac{\beta_3 - r_1}{(\lambda + 2\mu)(r_2 - r_1)}, \ g_3 = \frac{1}{\mu}, \ h_1 = -\frac{\beta_3}{\alpha_g(r_1 - r_2)}, \ h_2 = -\frac{\beta_3}{\alpha_g(r_2 - r_1)}$$

in which $r = \sqrt{(x_1 - y_1)^2 + (x_3 - y_3)^2}$ is the distance between field point $\boldsymbol{x} = (x_1, x_3)$ and source point $\boldsymbol{y} = (y_1, y_3)$. K_n is the modified Bessel function of the second kind of order n, and k_d is

$$k_1 = \sqrt{\frac{\beta_2\omega^2}{2} + \frac{\rho_g\omega^2 - \alpha_g\beta_3 + \sqrt{H}}{2(\lambda + 2\mu)}}, \ k_2 = \sqrt{\frac{\beta_2\omega^2}{2} + \frac{\rho_g\omega^2 - \alpha_g\beta_3 - \sqrt{H}}{2(\lambda + 2\mu)}}, k_3 = \sqrt{\omega^2\rho_g/\mu}$$

where

$$H = \left(\lambda\beta_2\omega^2 - \alpha_g\beta_3 + \rho_g\omega^2\right)^2 + 4(\lambda + \mu)\beta_2\omega^4(\mu\beta_2 - \rho_g) - 4\mu\alpha_g\beta_2\beta_3\omega^2$$

With the constitutive relationship, we have the traction fundamental solutions as

$$\begin{array}{c}\widetilde{t}^{s}_{ik} = \lambda\left[A' - B' - \frac{B}{r}\right]r_{,k}n_i + \mu\left[\left(A' - \frac{B}{r}\right)(r_{,n}\delta_{ik} + r_{,i}n_k)\right. \\ \left. -\frac{2B}{r}r_{,k}n_i + 2\left(-B' + \frac{2B}{r}\right)r_{,i}r_{,k}r_{,n}\right] \; i,k = 1,3,\end{array} \tag{A18}$$

where $r_{,i} = \frac{x_i - y_i}{r}$, $r_{,n} = r_{,1}n_1 + r_{,3}n_3$ and $(\bullet)'$ are the derivatives of $\bullet$ with respect to r.

For the fluid, the flux fundamental solutions are

$$\widetilde{q}_k = \frac{-\alpha_g}{\beta_3}\left[\frac{C}{r}n_k + \left(C' - \frac{C}{r}\right)r_{,k}r_{,n}\right], \; k = 1,3. \tag{A19}$$

(2) Fluid load

The singular load $\boldsymbol{F}^p = -\delta(\boldsymbol{x} - \boldsymbol{y})$ is applied to Equation (12). The variables are decomposed by the Helmholtz decomposition as

$$\widetilde{\boldsymbol{u}}^s = \nabla\varphi + \nabla \times \Psi, \tag{A20}$$

Taking Equations (A2) and (A20) into Equations (11) and (12), we have

$$(\lambda + 2\mu)\nabla^2\varphi + \omega^2\rho_g\varphi - \alpha_g p = 0, \tag{A21}$$

$$\mu\nabla^2\Psi + \omega^2\rho_g\Psi = 0, \tag{A22}$$

$$\nabla^2 p + \omega^2\beta_2 p - \beta_3\nabla^2\varphi = -\delta(\boldsymbol{x} - \boldsymbol{y}) \tag{A23}$$

Only Ψ is associated with Equation (A22). For simplicity, let $\Psi = 0$. The other two potentials are derived from

$$\nabla^2\begin{bmatrix}\varphi \\ p\end{bmatrix} + M\begin{bmatrix}\varphi \\ p\end{bmatrix} = \boldsymbol{h}\begin{bmatrix}0 \\ -\delta\end{bmatrix}, \tag{A24}$$

where M is the same as in Equation (A9), and $\boldsymbol{h} = (0,1)^T$. Then the eigenanalysis is based on

$$\begin{bmatrix}\varphi \\ p\end{bmatrix} = \phi_1\begin{bmatrix}1 \\ r_1'\end{bmatrix} + \phi_2\begin{bmatrix}1 \\ r_2'\end{bmatrix}. \tag{A25}$$

Recast Equation (A24) as

$$\nabla^2\phi_i + k_i^2\phi_i = -h_i\delta(\boldsymbol{x} - \boldsymbol{y}), \tag{A26}$$

where $h_i (i = 1,2)$ satisfies

$$\boldsymbol{h} = h_1\begin{bmatrix}1 \\ r_1'\end{bmatrix} + h_2\begin{bmatrix}1 \\ r_2'\end{bmatrix}. \tag{A27}$$

The solutions of Equation (A26) are

$$\phi_i(r) = \frac{h_i}{2\pi}K_0(\mathrm{j}k_i r). \tag{A28}$$

The 2D fundamental solutions can be derived via potentials and decomposition equations as

$$\widetilde{u}^s_{i4} = Dr_{,i}, \; i = 1,3, \tag{A29}$$

$$\widetilde{p}_4 = \frac{1}{2\pi}\sum_{d=1,2} r_d h_d K_0(z_d). \tag{A30}$$

Similarly, the fundamental solutions of the traction and flux are

$$\widetilde{t}_{i4} = \left[(\lambda + 2\mu)\frac{D}{r} + \lambda D'\right] n_i + 2\mu\left(-\frac{D}{r} + D'\right) r_{,i} r_{,n},\ i = 1, 3, \tag{A31}$$

$$\widetilde{q}_4 = \frac{\mathrm{j}\alpha_g r_{,n}}{2\pi\beta_3} \sum_{d=1,2} r_d h_d k_d K_1(z_d). \tag{A32}$$

Appendix B. The $\chi_1,\ldots,\chi_{10}$ of OIFs for 2D Saturated Poroelastic Problems

$$\chi_1 = \frac{g_1 + g_2 + g_3}{2}, \chi_3 = -\frac{1}{2\pi}\left(\frac{g_1 + g_2 - g_3}{2}\right), \chi_4 = -(\lambda + \mu)\left(\sum_{m=1,2} k_m^2 h_m\right),$$

$$\chi_2 = \frac{1}{2\pi}\left[\frac{g_1 + g_2 + g_3}{2}\overline{\tau} + \frac{g_1}{2}\ln\left(\frac{\mathrm{j}k_1}{2}\right) + \frac{g_2}{2}\ln\left(\frac{\mathrm{j}k_2}{2}\right) + \frac{g_3}{2}\ln\left(\frac{\mathrm{j}k_3}{2}\right) - \frac{g_1 + g_2 - g_3}{4}\right],$$

$$\chi_5 = \frac{1}{2\pi}\left[2(\lambda + \mu)\left(\sum_{m=1,2}\frac{k_m^2 h_m}{2}\left(\overline{\tau} + \ln\left(\frac{\mathrm{j}k_m}{2}\right)\right)\right) - \mu\sum_{m=1,2}\frac{k_m^2 h_m}{2}\right], \chi_6 = r_1 h_1 + r_2 h_2,$$

$$\chi_7 = \frac{1}{2\pi}\left[-(r_1 h_1 + r_2 h_2)\overline{\tau} - r_1 h_1 \ln\left(\frac{\mathrm{j}k_1}{2}\right) - r_2 h_2 \ln\left(\frac{\mathrm{j}k_2}{2}\right)\right], \chi_8 = -\frac{\alpha_g(r_1 g_1 + r_2 g_2)}{2\beta_3},$$

$$\chi_9 = \frac{\alpha_g}{2\pi\beta_3}\left[\frac{r_1 g_1 + r_2 g_2}{2}\left(\overline{\tau} - \frac{1}{2}\right) + \frac{r_1 g_1}{2}\ln\left(\frac{\mathrm{j}k_1}{2}\right) + \frac{r_2 g_2}{2}\ln\left(\frac{\mathrm{j}k_2}{2}\right)\right], \chi_{10} = \sum_{m=1,2} -\frac{\alpha_g r_m h_m}{\beta_3},$$

$\overline{\tau} = 0.57721566490153286$ is the Euler–Mascheroni constant.

References

1. Chen, G.; Yang, J.; Liu, Y.; Kitahara, T.; Beer, M. An energy-frequency parameter for earthquake ground motion intensity measure. *Earthq. Eng. Struct. Dyn.* **2022**, 1–14. [CrossRef]
2. Chen, G.; Li, Q.-Y.; Li, D.-Q.; Wu, Z.-Y.; Liu, Y. Main frequency band of blast vibration signal based on wavelet packet transform. *Appl. Math. Model.* **2019**, *74*, 569–585. [CrossRef]
3. Li, W.; Zhang, Q.; Gui, Q.; Chai, Y. A Coupled FE-Meshfree Triangular Element for Acoustic Radiation Problems. *Int. J. Comput. Methods* **2021**, *18*, 2041002. [CrossRef]
4. Chai, Y.; Li, W.; Liu, Z. Analysis of transient wave propagation dynamics using the enriched finite element method with interpolation cover functions. *Appl. Math. Comput.* **2022**, *412*, 126564. [CrossRef]
5. Pled, F.; Desceliers, C. Review and Recent Developments on the Perfectly Matched Layer (PML) Method for the Numerical Modeling and Simulation of Elastic Wave Propagation in Unbounded Domains. *Arch. Comput. Methods Eng.* **2022**, *29*, 471–518. [CrossRef]
6. Fu, Z.-J.; Xie, Z.-Y.; Ji, S.-Y.; Tsai, C.-C.; Li, A.-L. Meshless generalized finite difference method for water wave interactions with multiple-bottom-seated-cylinder-array structures. *Ocean Eng.* **2020**, *195*, 106736. [CrossRef]
7. Kythe, P.K. *Fundamental Solutions for Differential Operators and Applications*; Birkhauser: Basel, Switzerland, 1996.
8. Chen, C.S.; Karageorghis, A.; Smyrlis, Y.S. *The Method of Fundamental Solutions: A Meshless Method*; Dynamic Publishers: Atlanta, GA, USA, 2008.
9. Wei, X.; Chen, W.; Chen, B. An ACA accelerated MFS for potential problems. *Eng. Anal. Bound. Elem.* **2014**, *41*, 90–97. [CrossRef]
10. Chen, Z.; Sun, L. A boundary meshless method for dynamic coupled thermoelasticity problems. *Appl. Math. Lett.* **2022**, *134*, 108305. [CrossRef]
11. Wang, M.Z.; Xu, B.X.; Gao, C.F. Recent General Solutions in Linear Elasticity and Their Applications. *Appl. Mech. Rev.* **2008**, *61*, 030803–030820. [CrossRef]
12. Sun, L.; Zhang, C.; Yu, Y. A boundary knot method for 3D time harmonic elastic wave problems. *Appl. Math. Lett.* **2020**, *104*, 106210. [CrossRef]
13. Xu, W.-Z.; Fu, Z.-J.; Xi, Q. A novel localized collocation solver based on a radial Trefftz basis for thermal conduction analysis in FGMs with exponential variations. *Comput. Math. Appl.* **2022**, *117*, 24–38. [CrossRef]
14. Xi, Q.; Fu, Z.; Zhang, C.; Yin, D. An efficient localized Trefftz-based collocation scheme for heat conduction analysis in two kinds of heterogeneous materials under temperature loading. *Comput. Struct.* **2021**, *255*, 106619. [CrossRef]
15. Li, Z.C.; Lu, T.T.; Hu, H.Y.; Cheng, A.H.D. *Trefftz and Collocation Methods*; WIT Press: Boston, UK, 2008.
16. Sun, L.; Wei, X.; Chu, L. A 2D frequency-domain wave based method for dynamic analysis of orthotropic solids. *Comput. Struct.* **2020**, *238*, 106300. [CrossRef]

17. Karageorghis, A.; Lesnic, D.; Marin, L. A survey of applications of the MFS to inverse problems. *Inverse Probl. Sci. Eng.* **2011**, *19*, 309–336. [CrossRef]
18. Šarler, B. Solution of potential flow problems by the modified method of fundamental solutions: Formulations with the single layer and the double layer fundamental solutions. *Eng. Anal. Bound. Elem.* **2009**, *33*, 1374–1382. [CrossRef]
19. Chen, W. Singular boundary method: A novel, simple, meshfree, boundary collocation numerical method. *Chin. J. Solid Mech.* **2009**, *30*, 592–599.
20. Wei, X.; Chen, W.; Chen, B.; Sun, L. Singular boundary method for heat conduction problems with certain spatially varying conductivity. *Comput. Math. Appl.* **2015**, *69*, 206–222. [CrossRef]
21. Wei, X.; Chen, W.; Sun, L.; Chen, B. A simple accurate formula evaluating origin intensity factor in singular boundary method for two-dimensional potential problems with Dirichlet boundary. *Eng. Anal. Bound. Elem.* **2015**, *58*, 151–165. [CrossRef]
22. Wei, X.; Chen, W.; Fu, Z.J. Solving inhomogeneous problems by singular boundary method. *J. Mar. Sci. Technol. Taiwan* **2013**, *21*, 8–14. [CrossRef]
23. Wei, X.; Sun, L.; Yin, S.; Chen, B. A boundary-only treatment by singular boundary method for two-dimensional inhomogeneous problems. *Appl. Math. Model.* **2018**, *62*, 338–351. [CrossRef]
24. Wei, X.; Sun, L. Singular boundary method for 3D time-harmonic electromagnetic scattering problems. *Appl. Math. Model.* **2019**, *76*, 617–631. [CrossRef]
25. Wei, X.; Huang, A.; Sun, L. Singular boundary method for 2D and 3D heat source reconstruction. *Appl. Math. Lett.* **2020**, *102*, 106103. [CrossRef]
26. Wei, X.; Luo, W. 2.5D singular boundary method for acoustic wave propagation. *Appl. Math. Lett.* **2021**, *112*, 106760. [CrossRef]
27. Cheng, S.; Wang, F.; Li, P.-W.; Qu, W. Singular boundary method for 2D and 3D acoustic design sensitivity analysis. *Comput. Math. Appl.* **2022**, *119*, 371–386. [CrossRef]
28. Fu, Z.; Xi, Q.; Li, Y.; Huang, H.; Rabczuk, T. Hybrid FEM–SBM solver for structural vibration induced underwater acoustic radiation in shallow marine environment. *Comput. Methods Appl. Mech. Eng.* **2020**, *369*, 113236. [CrossRef]
29. Wei, X.; Rao, C.; Chen, S.; Luo, W. Numerical simulation of anti-plane wave propagation in heterogeneous media. *Appl. Math. Lett.* **2023**, *135*, 108436. [CrossRef]
30. Sun, L.; Wei, X. A frequency domain formulation of the singular boundary method for dynamic analysis of thin elastic plate. *Eng. Anal. Bound. Elem.* **2019**, *98*, 77–87. [CrossRef]
31. Sun, L.; Chen, W.; Cheng, A.H.D. Singular boundary method for 2D dynamic poroelastic problems. *Wave Motion* **2016**, *61*, 40–62. [CrossRef]
32. Sun, L.; Wei, X.; Chen, B. A meshless singular boundary method for elastic wave propagation in 2D partially saturated poroelastic media. *Eng. Anal. Bound. Elem.* **2020**, *113*, 82–98. [CrossRef]
33. Li, W.; Wang, F. Precorrected-FFT Accelerated Singular Boundary Method for High-Frequency Acoustic Radiation and Scattering. *Mathematics* **2022**, *10*, 238. [CrossRef]
34. Li, J.; Gu, Y.; Qin, Q.-H.; Zhang, L. The rapid assessment for three-dimensional potential model of large-scale particle system by a modified multilevel fast multipole algorithm. *Comput. Math. Appl.* **2021**, *89*, 127–138. [CrossRef]
35. Li, J.; Zhang, L.; Qin, Q. A regularized fast multipole method of moments for rapid calculation of three-dimensional time-harmonic electromagnetic scattering from complex targets. *Eng. Anal. Bound. Elem.* **2022**, *142*, 28–38. [CrossRef]
36. Li, J.; Fu, Z.; Gu, Y.; Qin, Q. Recent advances and emerging applications of the singular boundary method for large-scale and high-frequency computational acoustics. *Adv. Appl. Math. Mech.* **2022**, *14*, 315–343. [CrossRef]
37. Qu, W.; Chen, W.; Zheng, C. Diagonal form fast multipole singular boundary method applied to the solution of high-frequency acoustic radiation and scattering. *Int. J. Numer. Methods Eng.* **2017**, *111*, 803–815. [CrossRef]
38. Fu, Z.; Tang, Z.; Xi, Q.; Liu, Q.; Gu, Y.; Wang, F. Localized collocation schemes and their applications. *Acta Mech. Sin.* **2022**, *38*, 422167. [CrossRef]
39. Li, W. Localized method of fundamental solutions for 2D harmonic elastic wave problems. *Appl. Math. Lett.* **2021**, *112*, 106759. [CrossRef]
40. Zhu, T.; Zhang, J.D.; Atluri, S.N. A local boundary integral equation (LBIE) method in Comput. Mech., and a meshless discretization approach. *Comput. Mech.* **1998**, *21*, 223–235. [CrossRef]
41. Sun, L.; Fu, Z.; Chen, Z. A localized collocation solver based on fundamental solutions for 3D time harmonic elastic wave propagation analysis. *Appl. Math. Comput.* **2023**, *439*, 127600. [CrossRef]
42. Zhang, Y.; Dang, S.; Li, W.; Chai, Y. Performance of the radial point interpolation method (RPIM) with implicit time integration scheme for transient wave propagation dynamics. *Comput. Math. Appl.* **2022**, *114*, 95–111. [CrossRef]
43. Qu, W.; He, H. A spatial–temporal GFDM with an additional condition for transient heat conduction analysis of FGMs. *Appl. Math. Lett.* **2020**, *110*, 106579. [CrossRef]
44. Gao, X.-W.; Zheng, B.-J.; Yang, K.; Zhang, C. Radial integration BEM for dynamic coupled thermoelastic analysis under thermal shock loading. *Comput. Struct.* **2015**, *158*, 140–147. [CrossRef]
45. Kuhlman, K. Review of inverse Laplace transform algorithms for Laplace-space numerical approaches. *Numer. Algorithms* **2013**, *63*, 339–355. [CrossRef]
46. Xiao, J.; Ye, W.; Cai, Y.; Zhang, J. Precorrected FFT accelerated BEM for large-scale transient elastodynamic analysis using frequency-domain approach. *Int. J. Numer. Methods Eng.* **2012**, *90*, 116–134. [CrossRef]

47. Phan, A.V.; Gray, L.J.; Salvadori, A. Transient analysis of the dynamic stress intensity factors using SGBEM for frequency-domain elastodynamics. *Comput. Methods Appl. Mech. Eng.* **2010**, *199*, 3039–3050. [CrossRef]
48. Marrero, M.; Domínguez, J. Numerical behavior of time domain BEM for three-dimensional transient elastodynamic problems. *Eng. Anal. Bound. Elem.* **2003**, *27*, 39–48. [CrossRef]
49. Qu, W.; Gao, H.W.; Gu, Y. Integrating Krylov deferred correction and generalized finite difference methods for dynamic simulations of wave propagation phenomena in long-time intervals. *Adv. Appl. Math. Mech.* **2021**, *13*, 1398–1417.
50. Kausel, E.; Roësset, J.M. Frequency Domain Analysis of Undamped Systems. *J. Eng. Mech.* **1992**, *118*, 721–734. [CrossRef]
51. Tong, L.H.; Ding, H.B.; Yan, J.W.; Xu, C.; Lei, Z. Strain gradient nonlocal Biot poromechanics. *Int. J. Eng. Sci.* **2020**, *156*, 103372. [CrossRef]
52. Tong, L.; Yu, Y.; Hu, W.; Shi, Y.; Xu, C. On wave propagation characteristics in fluid saturated porous materials by a nonlocal Biot theory. *J. Sound Vib.* **2016**, *379*, 106–118. [CrossRef]
53. Biot, M.A. Theory of Propagation of Elastic Waves in a Fluid-Saturated Porous Solid. II. Higher Frequency Range. *J. Acoust. Soc. Am.* **1956**, *28*, 179–191. [CrossRef]
54. Lu, J.F.; Jeng, D.S.; Williams, S. A 2.5-D dynamic model for a saturated porous medium: Part I. Green's function. *Int. J. Solids Struct.* **2008**, *45*, 378–391. [CrossRef]
55. Wei, X.; Liu, D.; Luo, W.; Chen, S.; Sun, L. A half-space singular boundary method for predicting ground-borne vibrations. *Appl. Math. Model.* **2022**, *111*, 630–643. [CrossRef]
56. Gu, Y.; Chen, W.; Zhang, C.-Z. Singular boundary method for solving plane strain elastostatic problems. *Int. J. Solids Struct.* **2011**, *48*, 2549–2556. [CrossRef]
57. Ariza, M.P.; Dominguez, J. General BE approach for three-dimensional dynamic fracture analysis. *Eng. Anal. Bound. Elem.* **2002**, *26*, 639–651. [CrossRef]
58. Xiao, J.; Ye, W.; Wen, L. Efficiency improvement of the frequency-domain BEM for rapid transient elastodynamic analysis. *Comput. Mech.* **2013**, *52*, 903–912. [CrossRef]
59. Ba, Z.; Kang, Z.; Lee, V.W. Plane strain dynamic responses of a multi-layered transversely isotropic saturated half-space. *Int. J. Eng. Sci.* **2017**, *119*, 55–77. [CrossRef]